Optimal Fusion of Clutter-Suppression Residual's Magnitude and Phase for Distributed SAR-AMTI

Min Tian
Hangzhou Institution of Technology
Xidian University
Hangzhou, China,
tianmin@xidian.edu.cn

Bo Yuan
Shenzhen Research Institute
Tsinghua University
Shenzhen, China
boyuan@ieee.org

Shichao Chen
College of Artificial Intelligence
Nanjing Tech University
Nanjing, China
scchen0115@163.com

***Abstract*—This paper proposes an optimal fusion method for the magnitude and phase of clutter-suppression residuals in distributed synthetic aperture radar (SAR)-aerial moving target indication. In a distributed radar system with N M-channel SARs, the proposed approach first estimates the magnitude of M-channel clutter-suppression residuals and the interferometric phase between the first and last $M-1$-channel clutter-suppression residuals in each SAR as local tests. Based on the statistical estimation results, the receiver operator characteristic metrics are predicted, enabling the local detection by combining the magnitude and phase tests under a given probability of false alarm for each SAR. Finally, a global detection framework is developed to optimally fuse the local decisions from the N SARs. Simulation results are presented to validate the effectiveness in detecting weak targets.**

***Index Terms*—Distributed radar, aerial moving target detection, clutter-suppression residual's phase, optimal fusion**

I. Introduction

In synthetic aperture radar (SAR) aerial moving target indication (AMTI), clutter received from ground significantly spreads in Doppler due to the high platform speed, thereby masking moving targets. SAR systems generally deploy an antenna array with multiple phase centers along the track direction to suppress the ground clutter and detect weak moving targets in the endo-clutter region [1]–[3]. In practice, ground clutter is often heterogeneous, leading to a high probability of false alarm (Pfa) in many existing magnitude-based detection methods [4], [5]. Moreover, for aerial moving targets, such as unmanned aerial vehicles, the achievable coherence accumulation interval (CPI) is limited within the antenna's main lobe, resulting in a low signal-to-clutter-plus-noise ratio (SCNR), which poses significant challenge for target detection.

Existing solutions to SAR-AMTI in heterogeneous environments can be divide into two categories. The first focuses on reducing false alarms by improving clutter suppression performance [6]–[9]. The second explores different metrics to increase the dissimilarity between heterogeneous clutter and targets [10]–[16]. With the along-track interferometry (ATI) SAR techniques [10], [11], two-step detectors [12], and joint metrics combining the magnitude and phase of SAR interferograms [13] have been shown to improve the minimum discernible velocity (MDV) of targets. However, the ATI phases of low-SCNR targets are often affected by strong clutter signals, increasing the minimum discernible SCNRs required for successful target detection. Detectors incorporating the Degree of Radial-Velocity Consistency (DRVC) test [14] and those addressing filtering loss [15] have achieved improved minimum detectable SCNRs under heterogeneous conditions. Nevertheless, these methods often struggle when detecting targets with minimal residuals after clutter suppression, particularly those with small radial velocities.

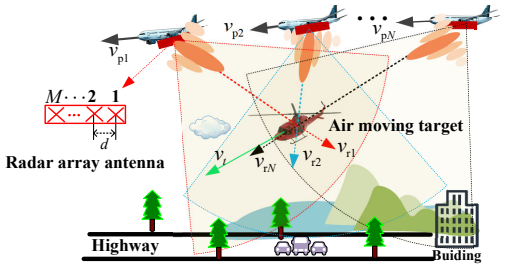

Fig. 1. Geometric relationship in the distributed SAR-AMTI system.

Distributed multichannel AMTI-SAR system, which employs several multi-channel SARs with a large spacing, can capture target information from different observation angles and provide increased spatial degrees of freedom (DoF) [17]–[19]. In this paper, a novel detector is proposed that optimally fuses the magnitude and phase of clutter-suppression residuals in distributed SAR-AMTI. Firstly, a two-step local detector is designed in each SAR by cascading the magnitude and interferometric phase tests. Next, global detection is achieved by optimally fusing these local detection decisions. Simulation results validate its effectiveness in detecting low-SCNR targets. Notations: T, $*$, and H represent the transposition, the conjugate operation, and the complex conjugate transposition, respectively. $\arg[\cdot]_{-\pi}^{\pi}$ denotes the phase of a complex number within the 2π cycle, and i is the imaginary unit with $\mathrm{i}^2=-1$.

II. Signal Model of Distributed Radar System

Consider a distributed AMTI-SAR system consisting of N M-channel SARs, where the physical spacing between any two adjacent channels in a SAR is d. The geometric

This work was supported in part by the National Natural Science Foundation of China under Grant 62431021, and in part by the China Aerospace Science and Technology Foundation under Grant Y22-CASTJJ-02. (Corresponding author: Bo Yuan)

relationship between this AMTI-SAR systems and an aerial moving target is shown in Fig. 1. During a CPI, SAR platforms move at velocities $v_{\mathrm{p}1}, v_{\mathrm{p}2}, \cdots, v_{\mathrm{p}N}$, respectively, and operate in a side-looking mode. For the target with velocity v_{t}, the radial velocity observed from the n-th SAR is denoted as $v_{\mathrm{r}n}$, $n = 1, 2, \cdots, N$. Suppose that each SAR transmits the orthogonal electromagnetic waves towards the same region, and receives echoes independently. After performing SAR imaging, platform motion compensation, and image registration and calibration, M SAR images with well-aligned coordinates are obtained for each SAR. Next, these SAR images are matched spatially based on their positions. For the n-th SAR, the complex signal in the pixel k of the m-th channel is denoted as $z_{n,m}(k)$, where $m = 1, \cdots, M$, $n = 1, 2, \cdots, N$, and $k = 1, \cdots, K$. As shown in Fig.1, radar echoes in a pixel inevitably contain ground clutter. Therefore, a binary hypothesis test for pixel k is defined as

$$\begin{aligned} \mathrm{H}_0 &: z_{n,m}(k) = c_{n,m}(k) + e_{n,m}(k) \\ \mathrm{H}_1 &: z_{n,m}(k) = s_{n,m}(k) + c_{n,m}(k) + e_{n,m}(k) \end{aligned} \tag{1}$$

where H_0 and H_1 represent the target-absent and target-present cases, respectively; $c_{n,m}(k)$ and $s_{n,m}(k)$ denote the clutter and target signals, respectively; $e_{n,m}(k) \sim \mathcal{N}^{\mathbb{C}}(0, \sigma_{\mathrm{e}}^2)$ denotes the Gaussian noise signal with zero mean and variance σ_{e}^2.

As the SARs are distributed far apart and observe the same target from different angles, the echoes show a low degree of correlation between SARs. However, within a single SAR, the echoes from M channels maintain strong coherence, enabling coherent signal processing. In this context, the random vector $\mathbf{z}_n(k)$ for the n-th SAR is expressed as

$$\mathbf{z}_n(k) = [z_{n,1}(k), z_{n,2}(k), \cdots, z_{n,M}(k)]^{\mathsf{T}}, \tag{2}$$

where $\mathbf{z}_n(k)$ represents the signal vector for M channels in the n-th SAR. Under the null hypothesis (H_0), the signal consists of clutter and noise: $\mathbf{z}_n(k) = \mathbf{c}_n(k) + \mathbf{e}_n(k)$. Under the alternative hypothesis (H_1), the signal also includes the target: $\mathbf{z}_n(k) = \mathbf{s}_n(k) + \mathbf{c}(k) + \mathbf{e}_n(k)$. In the above, $\mathbf{s}_n(k)$, $\mathbf{c}_n(k)$, and $\mathbf{e}_n(k)$ denote the target signal vector, clutter signal vector and noise signal vector, respectively.

For a moving target with a radial velocity $v_{\mathrm{r}n}$ in the n-th SAR, its Doppler shift $f_{\mathrm{t}n} = 2v_{\mathrm{r}n}/\lambda$ induces a phase shift of $2\pi f_{\mathrm{t}n}\frac{d/2}{V_n}$ during the array's traversal of the effective baseline $d/2$ [20], where λ is the radar wavelength. The target amplitudes from the M channels are assumed to be identical for focused target pixels. Therefore, $\mathbf{s}_n(k)$ is expressed as $\mathbf{s}_n(k) = \xi_{\mathrm{s}n}(k)\mathbf{a}_n(k)$, where $\xi_{\mathrm{s}n}(k)$ denotes the complex target amplitude for a single channel in the n-th SAR, and $\mathbf{a}_n(k)$ is the target spatial steering vector defined as

$$\mathbf{a}_n(k) = [1, \exp(\mathrm{i}2\pi f_{\mathrm{t}n}\frac{d}{2v_{\mathrm{p}n}}), \cdots, \exp(\mathrm{i}2\pi f_{\mathrm{t}n}\frac{(M-1)d}{2v_{\mathrm{p}n}})]^{\mathsf{T}}. \tag{3}$$

$\mathbf{c}_n(k)$ is modeled as the product of the complex amplitude $\xi_{\mathrm{c}n}(k)$ and the clutter spatial steering vector $\mathbf{b}_n(k)$: $\mathbf{c}_n(k) = \xi_{\mathrm{c}n}(k)\mathbf{b}_n(k)$, where $\mathbf{b}_n(k) \approx [1, \cdots, 1]^{\mathsf{T}}$ since the internal motion of the ground clutter is typically small. As ground clutter is usually heterogeneous with varied amplitudes due to changes in backscatter, a product model is used to model the amplitude variations in the n-th SAR [12], [21]:

$$\xi_{\mathrm{c}n}(k) = \Delta_n(k)\xi_{0n}(k) \tag{4}$$

where $\Delta_n(k) \in [0, \infty)$ is a texture variable representing the clutter amplitude changes, and $\xi_{0n}(k) \sim \mathcal{N}^{\mathbb{C}}(0, \sigma_n^2)$ denotes the homogeneous clutter amplitude following a complex Gaussian distribution with variance σ_n^2. For most heterogeneous backgrounds, the texture variable follows an inverse chi-square distribution [12], [21]

$$f_{\Delta_n}(\delta) = \frac{2(\chi_n - 1)^{\chi_n}}{\Gamma(\chi_n)}\delta^{-(2\chi_n+1)}\exp\left(-\frac{\chi_n - 1}{\delta^2}\right) \tag{5}$$

where χ_n denotes the degree of heterogeneity, and a smaller χ_n indicates greater heterogeneity; $\Gamma(\cdot)$ is the gamma function.

Note that the clutter parameters χ_n and σ_n^2, and the target parameters $\xi_{\mathrm{s}n}$ and $\mathbf{a}_n$ vary with $n = 1, 2, \cdots, N$.

III. Proposed detection method

The functional block diagram of the proposed method is illustrated in Fig. 2. In brief, multi-scale tests, including the magnitude tests $(T_1, T_2, \cdots, T_N)$ and the phase tests $(\varphi_1, \varphi_2, \cdots, \varphi_N)$, are constructed for each SAR. Then, the distribution characteristics of these tests under the two hypotheses are estimated, allowing the receiver operator characteristic (ROC) of each test to be predicted. For a given local detection Pfa, a two-step local detection is applied in each SAR. Finally, a global test β is formulated by optimally fusing these local decisions $u_1, \cdots, u_N$ with weights $a_1, \cdots, a_N$. The details are detailed as below.

A. Local Detection in Each SAR

1) Magnitude Detection: Adaptive matched filtering is employed in the range-Doppler domain for each SAR, where the optimum weighting vector for the n-th SAR is given by

$$\mathbf{w}_n(k) = \frac{\mathbf{R}_n^{-1}(k)\mathbf{a}_n(k)}{\mathbf{a}_n^{\mathsf{H}}(k)\mathbf{R}_n^{-1}(k)\mathbf{a}_n(k)}, \tag{6}$$

where $\mathbf{R}_n(k)$ is the clutter-plus-noise covariance matrix, estimated using L samples from the vicinity of pixel k as $\hat{\mathbf{R}}(k) = \frac{1}{L}\sum_{l=1}^{L}\mathbf{z}_n(l)\mathbf{z}_n{}^{\mathsf{H}}(l)$ [6], [7].

After clutter suppression, the residual signal in the n-th SAR is expressed as: $y_n(k) = |\mathbf{w}_n^{\mathsf{H}}(k)\mathbf{z}_n(k)|^2$. By normalizing the residual power by σ_n^2, the magnitude test is formulated as [12]

$$T_n(k) = \frac{\mathbf{w}_n^{\mathsf{H}}(k)\mathbf{z}_n(k)\mathbf{z}_n^{\mathsf{H}}(k)\mathbf{w}_n(k)}{\sigma_n^2} \tag{7}$$

which is compared against a threshold $\eta_{n,1}$ for detection. The threshold can be determined under a given Pfa ($P_{\mathrm{f}n1}$): $P_{\mathrm{f}n,1} = \int_{\eta_{n,1}}^{+\infty} f_{T_n}(t_n, \chi_n; \mathrm{H}_0)\mathrm{d}t_n$, where $f_{Tn}(t_n, \chi_n; \mathrm{H}_0)$ is the probability distribution function (pdf) of the magnitude test under H_0 [12]. For a moving target, assume that its maximum likelihood estimate of the magnitude test is ω_n, and the pdf for H_1 can be estimated as $f_{T_n}(t_n, \chi_n, \omega_n; \mathrm{H}_1)$. Accordingly, the probability of detection (Pd) can be computed as $P_{\mathrm{d}n,1} = \int_{\eta_{n,1}}^{+\infty} f_{T_n}(t_n, \chi_n, \omega_n; \mathrm{H}_1)\mathrm{d}t_n$.

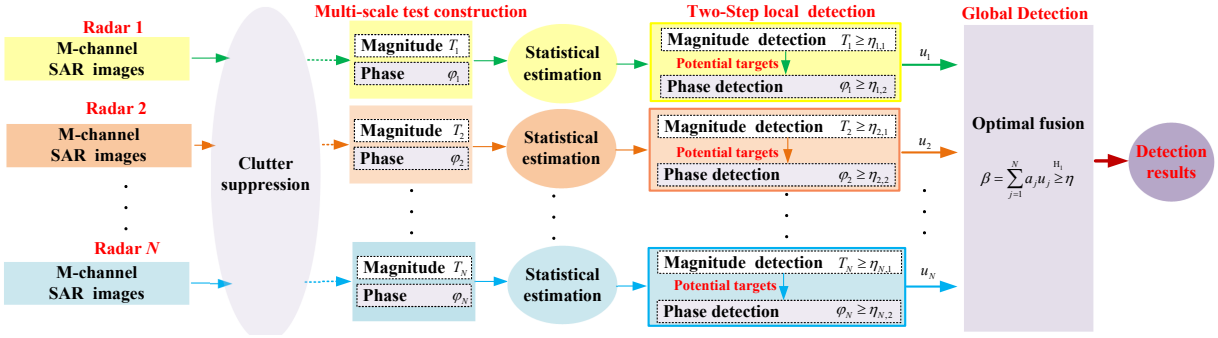

Fig. 2. Framework of the proposed detector.

2) Phase Detection: In the n-th SAR, the SAR images from the first and last $M-1$ channels are used to construct two data vectors for a given pixel k as follows

$$\mathbf{z}_{n1}(k) = [z_{n,1}(k), z_{n,2}(k), \cdots, z_{n,M-1}(k)]^{\mathsf{T}}, \tag{8a}$$

$$\mathbf{z}_{n2}(k) = [z_{n,2}(k), z_{n,3}(k), \cdots, z_{n,M}(k)]^{\mathsf{T}}. \tag{8b}$$

Here, $\mathbf{z}_{n1}(k)$ and $\mathbf{z}_{n2}(k)$ differ by a time delay of $d/(2v_{\mathrm{pn}})$. However, this time delay does not impact the spatial steering vector, allowing the same optimal weighting vector $\mathbf{w}_{n1}(k)$ to be applied to both data vectors for clutter rejection. The residual signals are then given by

$$y_{n1}(k) = \mathbf{w}_{n1}^{\mathsf{H}}(k)\mathbf{z}_{n1}(k), \quad y_{n2}(k) = \mathbf{w}_{n1}^{\mathsf{H}}(k)\mathbf{z}_{n2}(k). \tag{9a}$$

Based on the signal model in (1), we have $\mathbf{z}_{n1}(k) = \mathbf{c}_{n1}(k) + \mathbf{e}_{n1}(k)$ and $\mathbf{z}_{n2}(k) = \mathbf{c}_{n2}(k) + \mathbf{e}_{n2}(k)$ under H_0, while $\mathbf{z}_{n1}(k) = \mathbf{s}_{n1}(k) + \mathbf{c}_{n1}(k) + \mathbf{e}_{n1}(k)$ and $\mathbf{z}_{n2}(k) = \mathbf{s}_{n2}(k) + \mathbf{c}_{n2}(k) + \mathbf{e}_{n2}(k)$ under H_1. Here, $\mathbf{s}_{n1}$, $\mathbf{c}_{n1}$, and $\mathbf{e}_{n1}$ denote the target, clutter and noise signals in $\mathbf{z}_{n1}$, respectively, while $\mathbf{s}_{n2}$, $\mathbf{c}_{n2}$, and $\mathbf{e}_{n2}$ correspond to the target, clutter and noise signals in $\mathbf{z}_{n2}$, respectively. The time delay $\frac{d/2}{v_{\mathrm{pn}}}$ introduces a phase difference between $\mathbf{z}_{n1}(k)$ and $\mathbf{z}_{n2}(k)$, which propagates to the residual signals $y_{n1}(k)$ and $y_{n2}(k)$

$$\mathrm{H}_0: \quad y_{n1}(k) = y_{\mathrm{c1},n}(k) + y_{\mathrm{e1},n}(k), \tag{10a}$$

$$y_{n2}(k) = y_{\mathrm{c1},n}(k)\exp\left(\mathrm{i}2\pi\frac{f_{cn}(k)d}{2v_{\mathrm{pn}}}\right) + y_{\mathrm{e2},n}(k), \tag{10b}$$

$$\mathrm{H}_1: \quad y_{n1}(k) = y_{\mathrm{s1},n}(k) + y_{\mathrm{c1},n}(k) + y_{\mathrm{e1},n}(k), \tag{10c}$$

$$y_{n2}(k) = y_{\mathrm{s1},n}(k)\exp\left(\mathrm{i}2\pi f_{\mathrm{t}n}(k)\frac{d}{2v_{\mathrm{pn}}}\right) + y_{\mathrm{c1},n}(k)\exp\left(\mathrm{i}2\pi f_{cn}(k)\frac{d}{2v_{\mathrm{pn}}}\right) + y_{\mathrm{e2},n}(k), \tag{10d}$$

where $y_{\mathrm{c1},n}(k) = \mathbf{w}_{n1}^{\mathsf{H}}(k)\mathbf{c}_{n1}(k)$ and $y_{\mathrm{s1},n}(k) = \mathbf{w}_{n1}^{\mathsf{H}}(k)\mathbf{s}_{n1}(k)$ denote the residuals associated with the clutter and target signals, respectively; $y_{\mathrm{e1},n}(k) = \mathbf{w}_{n1}^{\mathsf{H}}(k)\mathbf{e}_{n1}(k)$ and $y_{\mathrm{e2},n}(k) = \mathbf{w}_{n1}^{\mathsf{H}}(k)\mathbf{e}_{n2}(k)$ denote the residuals of noise signals in $\mathbf{z}_{n1}(k)$ and $\mathbf{z}_{n2}(k)$, respectively, and $|y_{\mathrm{e1},n}(k)| \approx |y_{\mathrm{e2},n}(k)|$.

Next, by applying the complex interferometry over $y_{n1}(k)$ and $y_{n2}(k)$, we extract the interferometric phase by

$$\varphi_n(k) = \arg\left[y_{n1}(k)y_{n2}^*(k)\right]. \tag{11}$$

Under H_0, assume that a large stationary clutter residual signal is present, where $|y_{\mathrm{c1},n}| \gg |y_{\mathrm{e1},n}| \approx |y_{\mathrm{e2},n}|$ in (10a) and (10b). In this case, the interferometric phase $\varphi_n(k)$ in (11) approximates 0. Conversely, when a moving target signal is present alongside clutter and noise signals in the pixel, the clutter signal is nearly completely suppressed and the residual of the moving target signal typically exhibits a relatively large magnitude: $|y_{\mathrm{s1},n}(k)| \gg |y_{\mathrm{c1},n}(k)| > |y_{\mathrm{e1},n}(k)|$ as described in (10c) and (10d). Consequently, $\varphi_n(k) \approx 2\pi\frac{f_{\mathrm{t}n}(k)d}{2v_{\mathrm{pn}}} \neq 0$.

Based on this analysis, the phase detection is designed as

$$|\varphi_n(k)| \underset{\mathrm{H}_0}{\overset{\mathrm{H}_1}{\geq}} \eta_{n,2} \tag{12}$$

where $\eta_{n,2}$ is the detection threshold, and H_1 is declared if $|\varphi_n(k)| \geq \eta_{n,2}$; otherwise, H_0 is assumed. With the pdfs of the phase-based test estimated from data samples [14], $f_{\mathrm{p}n}(\varphi_n;\mathrm{H}_0)$ and $f_{\mathrm{p}n}(\varphi_n;\mathrm{H}_1)$, the threshold $\eta_{n,2}$ can be determined for a given Pfa ($P_{\mathrm{f}n,2}$) by $P_{\mathrm{f}n,2} = \int_{\eta_{n,2}}^{+\infty} f_{\mathrm{p}n}(\varphi_n;\mathrm{H}_0)\mathrm{d}\varphi_n$. Accordingly, Pd is computed by $P_{\mathrm{d}n,2} = \int_{\eta_{n,2}}^{+\infty} f_{\mathrm{p}n}(\varphi_n;\mathrm{H}_1)\mathrm{d}\varphi_n$.

In each SAR, if the cell satisfies both the magnitude and phase detection thresholds, $u_j = +1$; otherwise, $u_j = -1$, $j = 1, \cdots, N$. The values of Pd and Pfa ($P_{\mathrm{f}n}$ and $P_{\mathrm{d}n}$) can be approximated by $P_{\mathrm{f}n} = P_{\mathrm{f}n,1} \times P_{\mathrm{f}n,2}$, $P_{\mathrm{d}n} = P_{\mathrm{d}n,1} \times P_{\mathrm{d}n,2}$.

B. Global Detection

Based on the optimal fusion rule by Chair and Varshney [22], the fusion weights $a_1, \cdots, a_N$ are derived as [21]

$$a_j = \begin{cases} \log\dfrac{P_{\mathrm{d}j}}{P_{\mathrm{f}j}}, & \text{if } u_j = +1 \\ \log\dfrac{1-P_{\mathrm{f}j}}{1-P_{\mathrm{d}j}}, & \text{if } u_j = -1 \end{cases} \tag{13}$$

To proceed, the global detection is formulated as

$$\beta = \sum_{j=1}^{N} a_j u_j \underset{\mathrm{H}_0}{\overset{\mathrm{H}_1}{\geq}} \eta, \tag{14}$$

where $\eta = \log(P(\mathrm{H}_0)/P(\mathrm{H}_1))$ [21] with $P(\mathrm{H}_1)$ and $P(\mathrm{H}_0)$ being the prior probabilities for the hypotheses H_1 and H_0, respectively.

IV. Simulation Results

Simulation data are generated to evaluate target detection performance with following parameters: $N = 4$, $M = 8$, $\lambda = 0.25$ m, $d = 0.125$ m, $v_{\mathrm{p}1} = 120$ m/s, $v_{\mathrm{p}2} = 120$ m/s, $v_{\mathrm{p}3} = 100$ m/s, $v_{\mathrm{p}4} = 100$ m/s, $\chi_1 = 3$, $\chi_2 = 5$, $\chi_3 = 11$, $\chi_4 = 13$,

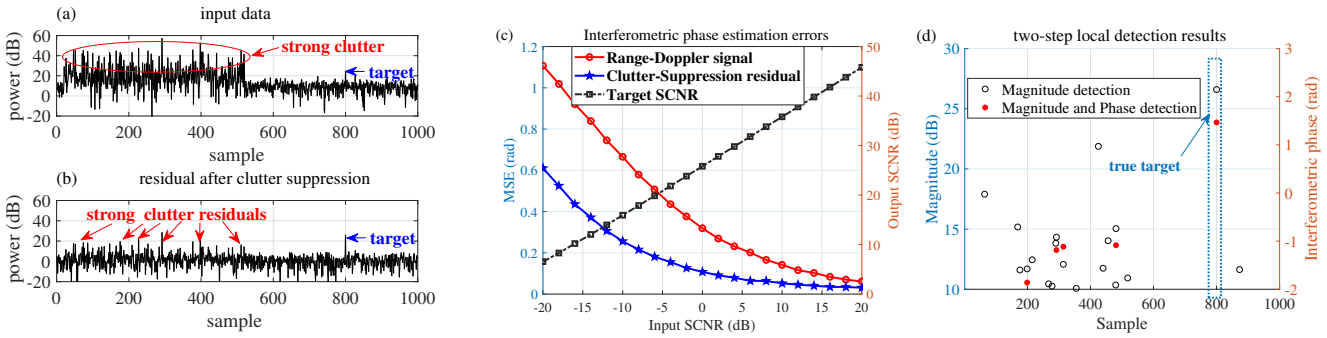

Fig. 3. Detection results in SAR 1: (a) magnitude of input SAR-image samples and (b) magnitude test based on clutter-suppression residuals; (c) interferometric phase estimation performance versus target SCNRS; (d) local two-step detection results with $P_{\text{fn},1} = 10^{-3}$ and $P_{\text{fn},2} = 10^{-1}$.

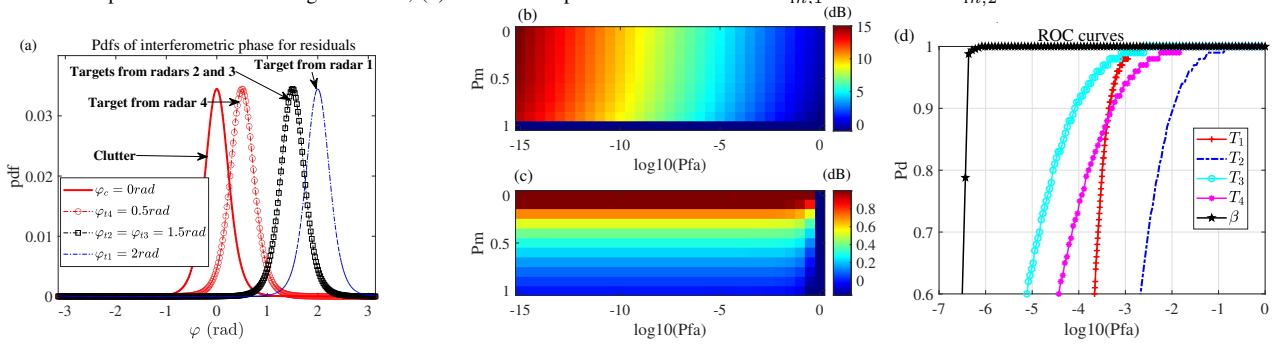

Fig. 4. Distributed SAR-AMTI results: (a) interferometric phase of clutter-suppression residuals across SARs; (b) optimal weights a_j versus local detection $P_{\text{f}j}$ and $P_{\text{m}j}$ for $u_j = +1$ and (c) optimal weights a_j versus local detection $P_{\text{f}j}$ and $P_{\text{m}j}$ for $u_j = -1$; (d) ROC curves.

$\omega_1 = 30$, $\omega_2 = 10$, $\omega_3 = 20$, $\omega_4 = 15$, $v_{\text{r}1} = 57$ m/s, $v_{\text{r}2} = 57$ m/s, $v_{\text{r}3} = 16$ m/s, and $v_{\text{r}4} = 63.67$ m/s. The clutter-to-noise ratios vary from 15 dB to 60 dB. In the simulation for SAR 1, there are 500 heterogeneous clutter samples with varied CNRs ranging from 15 dB to 60 dB, randomly distributed in the clutter background, while other 500 homogeneous clutter samples have a constant CNR of 15 dB. The texture parameter is estimated as $\hat{\chi}_1 = 3$. Additionally, the moving target is simulated with the parameters: $v_{\text{p}1} = 120$ m/s, $\omega_1 = 30$, and $v_{\text{r}1} = 57$ m/s, and added at the sample position 800. The input data and the outputs from clutter suppression for SAR 1 are compared in Figs. 3(a) and 3(b). It can be observed that most clutter can be effectively suppressed, although some strong clutter residuals persist due to heterogeneous clutter.

Next, based on the above clutter background of SAR 1, the mean square errors (MSE) for estimating target interferometric phases are computed for the dual-channel range-Doppler signals $z_{1,1}(k)$ and $z_{1,2}(k)$ (the classical ATI) [10], [11], and the clutter-suppression residuals $y_{11}(k)$ and $y_{12}(k)$((11)) via Monte Carlo simulation, respectively. The results for $v_{\text{r}1} = 57$ m/s are shown in Fig. 3(c). Compared with the classical ATI, the proposed interferometric phase demonstrates significantly improved accuracy for targets with low input SCNRs. Subsequently, the two-step local detection results for SAR 1 are shown in Fig. 3(d), with local Pfas set to as 10^{-3} and 10^{-1} for the magnitude and phase detection, respectively. Two tests for potential targets are displayed on the left and right vertical axes, respectively. In the results, the false alarms from the magnitude detection are largely mitigated by the complementary phase detection, while the true target is successfully identified with high precision. Based on the theoretical statistics in [14], the pdfs of the interferometric phases from the clutter-suppression residuals for different SARs are illustrated in Fig. 4(a). It highlights the variability of target signatures across radars and the statistical differences between the clutter and target residuals in the interferometric phase. In the optimal fusion process, the schematic diagrams of the optimal weights a_j versus local detection probabilities $P_{\text{f}j}$ and $P_{\text{m}j} = 1 - P_{\text{d}j}$ are shown in Fig. 4(b) and Fig. 4(c). It is evident that, the optimal fusion weights increase with higher detection reliability, confirming that the fusion rule adaptively prioritizes more reliable local decisions. Finally, ROC curves in Fig. 4(d) indicate that the proposed method achieves a higher Pd compared with single-radar magnitude detections under the same Pfa.

V. Conclusion

The proposed method utilizes both the magnitude and interferometric phase of clutter-suppression residuals for aerial moving target detection in distributed synthetic aperture radar (SAR) systems. The approach incorporates a local two-step detection for each SAR, combining the magnitude and phase tests sequentially. Subsequently, the local decisions from all SARs are fused using optimally derived weights to formulate a global detection. Simulation results demonstrate that the proposed method can effectively reduce false alarms in heterogeneous environments by leveraging the interferometric phase of the residuals. Moreover, by utilizing multi-angle sensing information inherent in distributed SAR systems, the proposed technique significantly enhances the target detection probability.

REFERENCES

[1] R. Klemm, "Adaptive clutter suppression for airborne phased array radars," *IEE Proceedings F - Communications, Radar and Signal Processing*, vol. 130. no. 1, 2008, pp.125-132.

[2] D. Cerutti-Maori, I. Sikaneta, "A Generalization of DPCA Processing for Multichannel SAR/GMTI Radars," *IEEE Transactions on Geoscience and Remote Sensing*, vol. 52, num. 1, 2013, pp. 560-572.

[3] D. Cerutti-Maori, I. Sikaneta, and C. H. Gierull, "Optimum SAR/GMTI processing and its application to the radar satellite RADARSAT-2 for traffic monitoring," *IEEE Transactions on Geoscience and Remote Sensing*, vol. 50, no. 10, pp. 3868–3881, 2012.

[4] Kim, Donghoon and Park et al,"Accurate Clutter Synthesis for Heterogeneous Textures and Dynamic Radar Environments," *IEEE Transactions on Aerospace and Electronic Systems*, vol. 58, no. 4, 2022, pp. 3427-3445.

[5] Z. Dai, P. Wang, H. Wei, and Y. Xu, "Adaptive detection with constant false alarm ratio in a non-Gaussian noise background," *IEEE Communications Letters*, vol. 23, no. 8, pp. 1369–1372, 2019.

[6] F. Gini and M. Rangaswamy, "Knowledge based radar detection, tracking and classification," *Wiley-Interscience*, 2008.

[7] K. Sun, H. Meng, Y. Wang, and X. Wang, "Direct data domain STAP using sparse representation of clutter spectrum," *Signal Processing*, vol. 91,no. 9, pp. 2222–2236, 2011.

[8] W. Zhang, R. An, N. He, Z. He, and H. Li, "Reduced dimension STAP based on sparse recovery in heterogeneous clutter environments," *IEEE Transactions on Aerospace and Electronic Systems*, vol. 56, no. 1, pp.785–795, 2020.

[9] P. Huang, H. Yang, Z. Zou, X. -G. Xia, G. Liao and Y. Zhang, "Range-Ambiguous Sea Clutter Suppression for Multichannel Spaceborne Radar Applications Via Alternating APC Processing," *IEEE Transactions on Aerospace and Electronic Systems*, vol. 59, no. 5, pp. 6954-6970, Oct. 2023.

[10] R. Romeiser, S. Suchandt, H. Runge, U. Steinbrecher, and S. Grunler, "First analysis of terrasar-x along-track insar-derived current fields," *IEEE Transactions on Geoscience and Remote Sensing*, vol. 48, no. 2,pp. 820–829, 2010.

[11] A. Budillon, C. H. Gierull, V. Pascazio, and G. Schirinzi, "Along track interferometric SAR systems for ground-moving target indication: Achievements, potentials, and outlook," *IEEE Geoscience and Remote Sensing Magazine*, vol. 8, no. 2, pp. 46–63, 2020.

[12] C. H. Gierull, I. Sikaneta, and D. Cerutti-Maori, "Two-step detector for radarsat-2's experimental GMTI mode, *IEEE Transactions on Geoscience and Remote Sensing*,vol. 51, no. 1, pp. 436–454, 2013.

[13] G. Gao and G. Shi, "The cfar detection of ground moving targets based on a joint metric of SAR interferogram's magnitude and phase," *IEEE Transactions on Geoscience and Remote Sensing*, vol. 50, no. 9, pp. 3618–3624, 2012.

[14] B. Liu, K. Yin, Y. Li, F. Shen, and Z. Bao, "An improvement in multichannel sar-gmti detection in heterogeneous environments," *IEEE Transactions on Geoscience and Remote Sensing*, vol. 53, no. 2, pp.810–827, 2015.

[15] M. Tian, Z. Yang, H. Xu, G. L.iao, and W. Wang, "An enhanced approach based on energy loss for multichannel SAR-GMTI systems in heterogeneous environment," *Digital Signal Processing*,vol. 78, pp. 393–403, 2018.

[16] L. Wang et al., "A Linearly Continous False Alarm Removing Method in a Multichannel SAR-GMTI System," *IGARSS 2024 - 2024 IEEE International Geoscience and Remote Sensing Symposium*, Athens, Greece, 2024, pp. 6802-6806.

[17] R. R. Tenney and N. R. Sandell, "Detection with distributed sensors," *IEEE Transactions on Aerospace and Electronic Systems*, vol. AES-17, no. 4, pp. 501–510, 1981.

[18] J. Chen, J. Ma, P. Huang et al., "Approach for AMTI Formation Design in a Distributed Space-based Radar System," *IGARSS 2024 - 2024 IEEE International Geoscience and Remote Sensing Symposium*, Athens, Greece, 2024, pp. 3740-3743.

[19] P. Chen, L. Zheng, X. Wang, H. Li and L. Wu, "Moving Target Detection Using Colocated MIMO Radar on Multiple Distributed Moving Platforms," *IEEE Transactions on Signal Processing*, vol. 65, no. 17, 1 Sept.1, 2017, pp. 4670-4683.

[20] B. C. Liu, T. Wang, Y.K. Li, et al, "Effects of Doppler Aliasing on Baseline Estimation in Multichannel SAR-GMTI and Solutions to Address These Effects," *IEEE Transactions on Geoscience and Remote Sensing*, vol.52, no. 10, 2014, pp. 6471-6487.

[21] M. Tian and B. Liao, "Optimal Fusion-Based Target Detection With Multichannel ATI SAR," *IEEE Transactions on Geoscience and Remote Sensing*, vol. 62, pp. 1-15, 2024, Art no. 5228015.

[22] Z. Chair and P. K. Varshney, "Optimal Data Fusion in Multiple Sensor Detection Systems," *IEEE Transactions on Aerospace and Electronic Systems*, vol. AES-22, no. 1, pp. 98-101, Jan. 1986.